Muon spin spectroscopy evidence of a charge density wave in magnetite below the Verwey transition

M. Bimbi, G. Allodi, and R. De Renzi
Dipartimento di Fisica and Unità CNISM di Parma, Università degli Studi di Parma, Viale G.P. Usberti, 7A, I-43100 Parma, Italy

C. Mazzoli
ESRF, 6 rue Jules Horowitz, 38043 Grenoble, France

H. Berger
Institut de Physique de la Matire Complexe, EPFL, CH-1015 Lausanne, Switzerland

(Received 26 November 2007; published 14 January 2008)

We present muon spectroscopy data on a Fe_3O_4 single crystal, revealing different spin precession patterns in five distinct temperature ranges. A careful analysis of the local field and its straightforward modeling obtains surprisingly good agreement with experiments only if a very specific model of localized charges violating Anderson condition, and a correlated muon local dynamics is implemented. Muon evidence for fluctuations just above the Verwey temperature, precursor of the low temperature charge localized state, is provided.

DOI: 10.1103/PhysRevB.77.045115 PACS number(s): 71.30.+h, 71.45.Lr, 72.25.−b, 76.75.+i

I. INTRODUCTION

The real nature of the charge ordered state in many transition metal oxides, notably manganites[1] and magnetite,[2–4] is still controversial. Do they correspond to distinct integer localized cation charges or to a much smaller charge disproportionation? The issue is of course also relevant to the nature of the carriers in the highly spin polarized metallic regimes of these oxides, which are of great interest for potential spintronic applications.

The half-metallic character of magnetite, i.e., the fact that majority and minority-spin subbands are partially and completely filled, respectively, was recently pointed out[5] and attracted renewed interest[6–9] to this prototypic magnetic material. In the original Verwey model,[10] questioned recently,[2,3,11] it is due to charge delocalization between equal fractions of Fe^{2+} and Fe^{3+} ions, occupying the octahedral B sublattice of the inverse spinel structure, AB_2O_4, whereas Fe^{3+} ions stably occupy the tetrahedral A sublattice. The metal-insulator transition takes place at T_V (above 120 K in good samples[12]). A and B also correspond to the ferrimagnetic sublattices (Fig. 1), hence all the B-site spins are fully aligned, with easy axis along [111] above T_V. Below T_V, the spin is parallel along [001]. The B sites form a pyrochlore network of corner-sharing tetrahedra [henceforth, the B pyrochlore units (B_{pcu})].

Assuming, with Verwey, localized Fe^{3+} and Fe^{2+} at B sites in the insulating state, Anderson[13] noticed that the rather low T_V implies a small activation energy. He proposed that instantaneous local charge configurations, both above and below T_V, must satisfy a condition of minimum local energy, where each B_{pcu} contains two Fe^{3+} and two Fe^{2+} ions.

However, both magnetic moments[2] (Table I) and localized charges below T_V do not correspond experimentally to those expected of Fe^{3+} and Fe^{2+}. Bond valence sums[2] and resonant x-ray scattering[15] indicate that the charge contrast among the B-site cations cannot be more than $0.2e$. Joint refinement[2,14] of x-ray and neutron diffraction data in the approximate $P2/c$ symmetry relaxes the Anderson condition, supporting a model (hereafter, the Wright model) with $Fe^{2.4+}$ and $Fe^{2.6+}$ ions on the B sites. It corresponds to a [001] charge density wave (CDW), as shown in Fig. 7 of Ref. 14. The CDW is composed of two types of B_{pcu}: one with $Fe^{2.4+}/Fe^{2.6+}$ occupancy ratio of 1:3 and the second, shown in Fig. 1, with occupancy ratio of 3:1. Direct evidence of a large symmetry reduction below T_V comes also from NMR[16,17] which identifies 16 nonequivalent B cations. NMR also reveals a distinct spin reorientation transition,[16] at $T_R \approx 126$ K, slightly above T_V.

Muon spin rotation (μSR) spectroscopy provides a broadband local magnetic probe, alternative to NMR. Implanted muons end up in an interstitial site with a characteristic local magnetic field and, like in NMR, the reduced symmetry of the local environment may be detected directly from the spin precessions. The present paper reports on zero field muon data which were already partially published with a very preliminary analysis,[18] improved here to provide a full muon site assignment. A rather detailed picture of charge localization emerges, which fully supports the CDW model.

We describe experimental method and results in Sec. II, the site assignment strategy assisted by calculations of lattice sums is presented in Sec. III and discussed in Sec. IV.

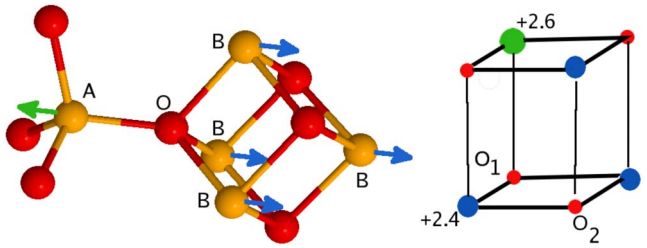

FIG. 1. (Color online) Spinel unit with A and B Fe ions and the $T > T_V$ spin structure (left); low charge B_{pcu} (right) from Ref. 14 with red O, blue $Fe^{+2.4}$, and green $Fe^{+2.6}$.

TABLE I. Magnetic moments, in μ_B, from Ref. 2 (cubic cell).

Temperature	Fe_A	Fe_B	S direction
$T>T_V$	−4.20	3.97	[111]
$T<T_V$	−4.44	4.17	[100]

II. EXPERIMENTAL RESULTS

A. Methods

We performed μSR experiments in zero applied magnetic field on a high quality single crystal at the Paul Scherrer Institut, on the GPS and Dolly spectrometers. This large crystal (cut as a platelet, roughly $5\times4\times1$ mm^3) displays a Verwey transition around $T_V=121$ K, confirmed by the μSR analysis which detects $T_V=120.9(4)$. Superconducting quantum interference device magnetometry on a fragment of our sample showed $T_V=122(1)$ K.

The Verwey transition temperature qualifies our sample as state of the art, although it has been pointed[12] out that in very best samples, and depending upon the details of thermal history, the Verwey transition may reach up to 125 K, very close to the reorientation transition $T_R=126$ K, determined[16] with NMR. However, large shifts of the transition temperatures are recorded when stress is applied to the sample and even with the establishing of thermal gradients. The cooling of our large μSR single crystal was quite rapid (15 min from RT to 10 K), hence we cannot exclude that parts of our sample developed a narrow distribution of Verwey temperatures, of which the lowest bound is $T_V=120.9(4)$ K.

Different geometries were employed, but the cubic symmetry of the $T>T_V$ phase makes them equivalent for the detection of precessing muon spin components in unmagnetized samples, both above and below T_V. The time dependent asymmetry of the muon decay in a given set of detectors mirrors the spin precessions and it is fitted to a sum of relaxing oscillating components,

$$\mathcal{A}(t)=\frac{2}{3}\mathcal{A}_0\sum_j f_j\cos(2\pi\gamma B_{\mu j}t)\exp(-t^2\sigma_j^2/2), \qquad (1)$$

where $\gamma=135.5$ MHz/T is the muon magnetogyric ratio, $\mathcal{A}_0$ the total initial muon asymmetry, and $B_{\mu j},\sigma_j/2\pi\gamma$, respectively, the local field intensity and its second moment for each transverse muon fraction f_j. Additional nonprecessing terms account for local field components parallel to the initial muon spin direction, which, in cubic and pseudocubic symmetries, amount to an initial asymmetry of $\mathcal{A}_0/3$.

Experiments[19,20] with previous generation facilities and much lower statistics measured only one precession frequency γB_μ above T_V and none below. We detect here up to three frequencies both above and below T_V. Their identification is guided by a fast Fourier transform (FFT) of the time domain asymmetries, which may be repeated with different apodization windows to isolate components with diverse relaxation rates. The FFT is applied also to the residues of the fit, to ensure that all terms have been correctly fitted, until a reduced $\chi_r^2\leq1.1$ is obtained.

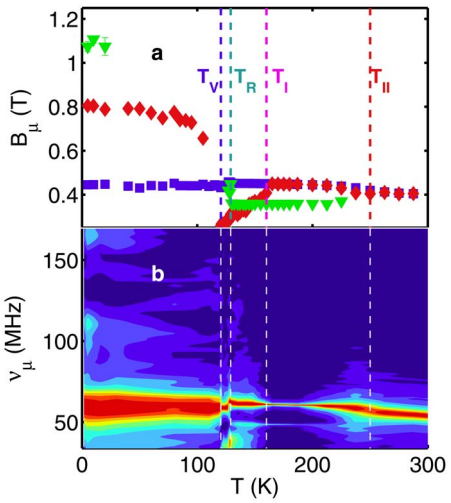

FIG. 2. (Color online) Comparison between fitted features (panel a, equivalent to Fig. 5) and the color map of the fast Fourier transform amplitudes of the muon asymmetries versus temperature (panel b); each FFT spectrum is normalized to its maximum.

B. Results

Figure 2(b) shows a color map of the FFT amplitude versus temperature and frequency. This figure, where spectra at each temperature are normalized to their maximum amplitude, provides a qualitative picture, revealing up to three components. The precession frequencies in this plot are proportional to field intensities, but the amplitudes are only indicative, since when both slow and fast relaxing components are present, the apodization enhances one over the other, depending on its time window. The three lowest temperature components are, for instance, more evident in the FFT spectrum shown separately in Fig. 3. The higher-frequency ones, barely visible in Fig. 2, disappear from the color plot above 10 K, which is due to a lower statistics of these data sets and to the discreteness of the color coding.

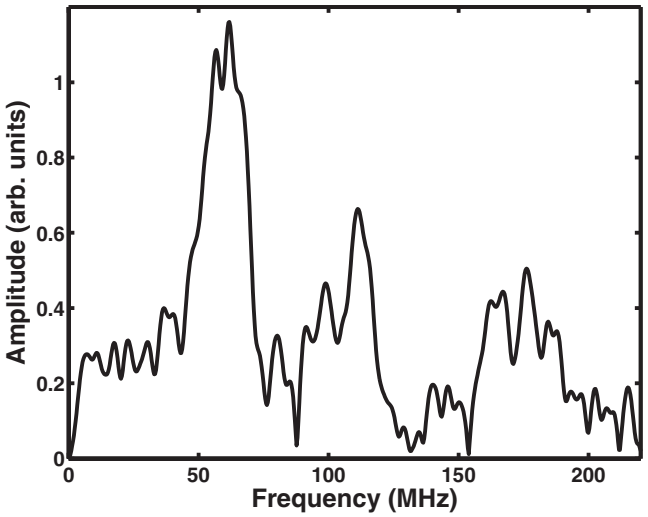

FIG. 3. FFT amplitudes at $T=5$ K, with Gaussian apodization ($\sigma=8.0\times10^6$ s^{-1}).

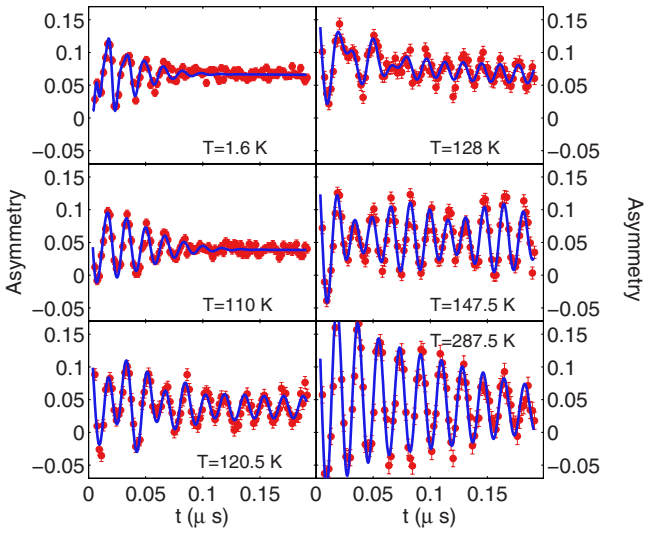

FIG. 4. (Color online) Muon asymmetry in zero external field at selected temperatures, with best fit.

Figure 4 displays the time dependence of a six representative muon asymmetries, between 1.6 and 300 K, together with the best fit precession patterns according to Eq. (1), obtained by the described procedure. The temperature behavior of the local field intensities $B_{\mu j}$ from the best fit is shown in Fig. 5. The fitted frequencies of this figure agree very well with the pattern from the FFT, as it may be seen by comparing Figs. 2(a) and 2(b).

We identify five distinct temperature intervals from the behavior of the internal fields depicted in Fig. 5,

(i) For $T > T_{\mathrm{II}} = 250$ K, $\boldsymbol{S} \| [111]$, only one field, $B_{\mu} \approx 0.42$ T, is detected; the best fit has two components: one with fast (red diamonds) and one with slow relaxations (blue squares).

(ii) For $T_{\mathrm{I}} = 160$ K $< T < T_{\mathrm{II}}$, $\boldsymbol{S} \| [111]$, two fields are detected, $B_{\mu 1} \approx 0.36$ T (green triangles) and $B_{\mu 2} \approx 0.43$ T (blue squares), with $f_2/f_1 = 3$; red diamonds correspond again to the same field $B_{\mu 2} \approx 0.43$ T, but with faster relaxation.

(iii) For $T_R < T < T_{\mathrm{I}}$, a third extra field $B_{\mu 3}$ is detected, decreasing with temperature from roughly $(B_{\mu 1} + 3B_{\mu 2})/4$ toward an extrapolated value of 0.25 T, with fractions $f_3/(f_1 + f_2) \approx 1$.

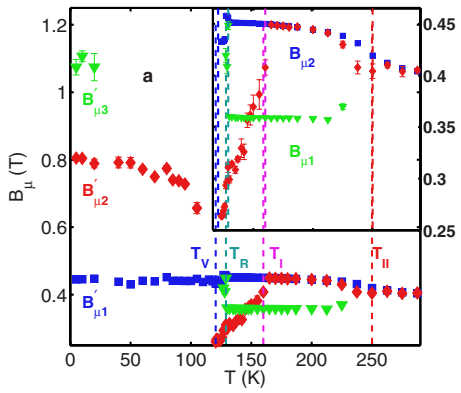

FIG. 5. (Color online) Temperature dependence of the detected local muon fields B_{μ}; the inset is a blow-up for $T > T_V$.

(iv) A sharp change takes place around $T_R = 126(1)$ K, where, following the spin reorientation[16] from $\boldsymbol{S} \| [111]$ ($T > T_R$) to $\boldsymbol{S} \| [001]$ ($T < T_R$), $B_{\mu 1}$ and $B_{\mu 2}$ collapse into $B'_{\mu 1} = 0.435$ T, while $B_{\mu 3}$ still survives.

(v) For $T < T_V$, three fields are detected, $B'_{\mu 1}$, $B'_{\mu 2} \approx 0.75$ T and $B'_{\mu 3} \approx 1.06$ T, with comparable fractions $\approx 1/3$ and large relaxation rates $\sigma_1 < \sigma_2 < \sigma_3$.

In order to understand this diverse behavior, we must address the issue of muon localization and site assignment, which was already attempted in earlier μSR work.[19,20] A unique muon interstitial site assignment justifies all the features [(i)–(v)]. We concentrate here just on the field intensities and fractions, whereas finer details, such as relaxations, will be published elsewhere.[21]

III. SITE ASSIGNMENT

We describe below the calculation enabling our site assignment. Its identification is first independently obtained from a simple electrostatic point-charge calculation, based on the notion that muons bind to oxygen[19,22] as a light hydrogen isotope, with bond lengths approximately equal to $r_{\mu} = 1.1$ Å. We therefore search for the minima of the electrostatic energy for a positive charge constrained on a sphere centered on oxygen ions. We then check that the local magnetic field in the close vicinity of these minima agrees with the measured fields. Since the point-charge model is very crude, the aim of the electrostatic determination of the muon minima is to catch the symmetry of the full potential, i.e., to identify the approximate positions, and, more importantly, the degeneracy of the minima, seeking approximate agreement with experimental field values (within 10%).

The full calculations of the electrostatic potential $\phi_e(\boldsymbol{r})$ and dipolar field $\boldsymbol{B}_d$ are performed over Lorentz spheres of radius $r_L = 40$ Å, which grants a relative numerical accuracy of better than 0.02 and 3×10^{-4}, respectively. However, we verified that values of $\phi_e(\boldsymbol{r})$ within a few percent of those from the full sums are obtained considering just the asymmetric subunit shown in Fig. 1 (left). The minima are identified in this simplified calculation, which allows a much finer scan of the potential $\phi_e(\boldsymbol{r})$ over the sphere $\mathcal{S}(r_{\mu})$ centered on a single oxygen, labeled O in Fig. 1. Minima around other O ions are then obtained by crystal symmetry operations. Magnetic dipolar fields are finally calculated in each magnetically nonequivalent site with the full lattice sums. Within the required accuracy of 10%, the above approximations disregard the small distortion of the low temperature phase, and dipolar sums are performed always in the cubic lattice. We further ignore the small lattice linear thermal expansion[23] ($\approx 10^{-4}$ at room temperature).

The minima of the electrostatic potential ϕ_e constrained on the sphere $\mathcal{S}(r_{\mu})$ centered on oxygen are shown in Fig. 6(3). Three equivalent minima (labeled a, b, and c) are connected by a low potential path, separated by shallow barriers. They form a network in the lattice, as shown in Fig. 6(4).

For an unmagnetized sample in zero external field, the total local magnetic induction at a specific muon site[24] is

$$\boldsymbol{B}_{\mu} = \boldsymbol{B}_d + \boldsymbol{B}_{hf} + \boldsymbol{B}_L, \tag{2}$$

where $\boldsymbol{B}_d$ is given by dipolar sums within a Lorentz sphere, with the known magnetic moments (Table I), $\boldsymbol{B}_L$ is the con-

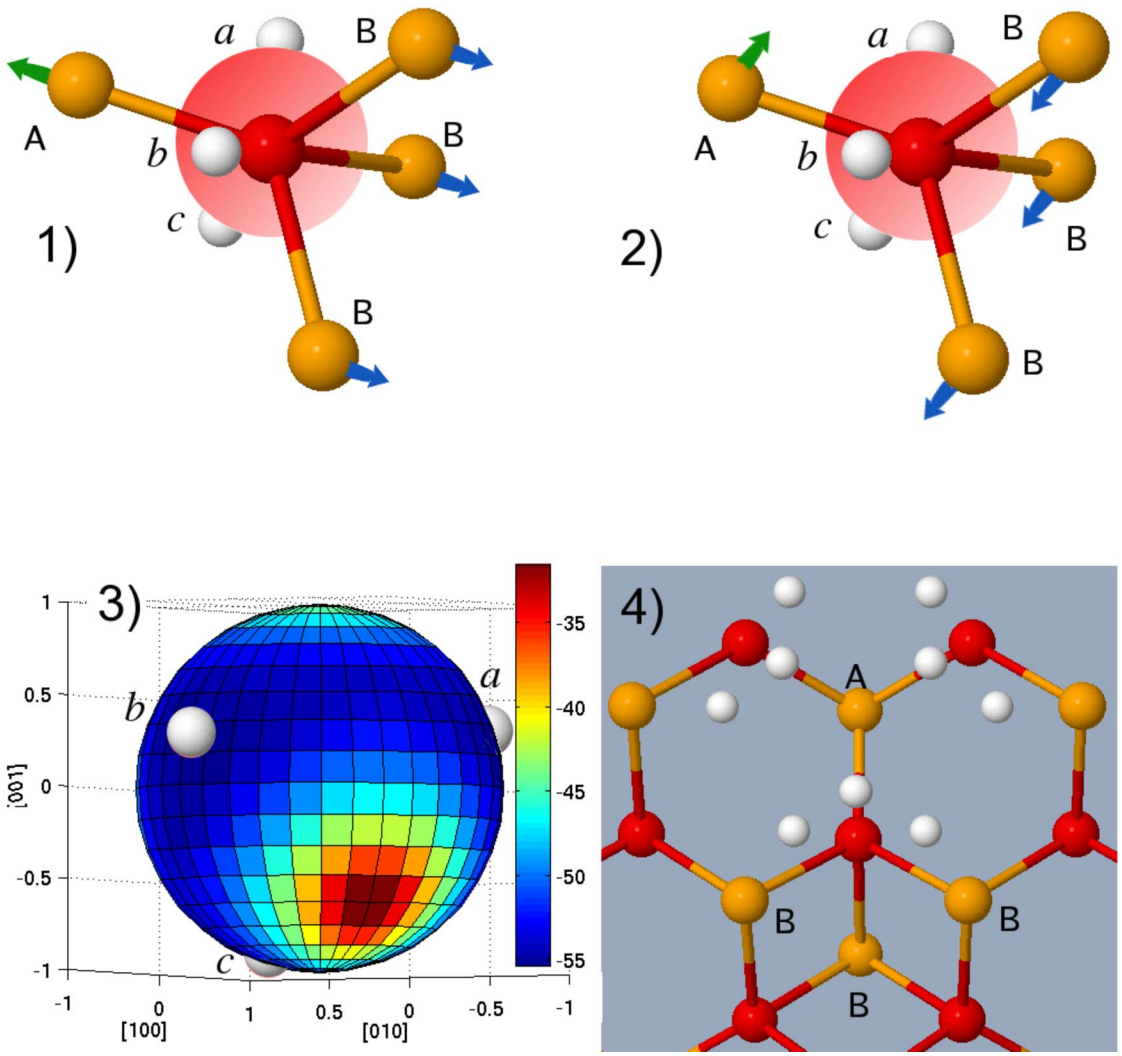

FIG. 6. (Color online) [(1) and (2)] White balls are μ sites (a,b,c) around a sphere $\mathcal{S}$ (color gradient) of radius 1.1 Å, centered on oxygen (red), on which $\phi_e(r)$ is calculated; Fe_A and Fe_B (yellow). Spin orientation distinguishes (2) three times as frequent as (1). (3) Map of the electrostatic potential ϕ_e on $\mathcal{S}$, showing three equivalent minima (a,b,c) with low valleys in between. (4) Muon site network seen from [011]-O ions lie in the (011) plane.

tribution from the Lorentz countersphere $[B_L(T)=\frac{\mu_0}{3}M(T)$, with $M(0)$ equal to domain magnetization, $B_L(0)=0.21$ T], and $\boldsymbol{B}_{hf}$ an *a priori* unknown hyperfine contribution, also parallel to the domain magnetization $\boldsymbol{M}$, originating from an isotropic coupling[25] to the unpaired spins of neighbor Fe ions. The coupling is mediated by the O ion to which the muon binds, and the contact contribution from the σ oxygen-muon bond is largely dominant. Therefore, the hyperfine field and the Lorentz field both lie in the direction of the domain magnetization.

The three muon sites around each oxygen are crystallographically equivalent, hence they experience the same hyperfine field, but the electron magnetic moment direction breaks the symmetry, yielding distinct dipolar fields.

IV. DISCUSSION

A. Above T_V

We can now discuss our experimental results, starting from high temperatures, $T>T_{\mathrm{II}}$, where one value of $|\boldsymbol{B}_\mu|$ is detected. As it was already recognized by Boekema *et al.*,[19] a single value implies that the muon must be hopping among all equivalent sites. Indeed, since the spin orientation at the B site, $\boldsymbol{S}\|[111]$, distinguishes two families of O ions, as shown in Figs. 6(1) and 6(2), six large distinct local fields $(j=1,2$ and $\alpha=a,b,c)$ are predicted and no value of the hyperfine field $\boldsymbol{B}_{hf}$ can reconcile all of them with the experiment without invoking muon hopping, as we show below in detail.

Direct inspection reveals that dipolar sums (for their tensorial nature) yield three different results (a, b, and c) for (1) muon sites where the domain magnetization $\boldsymbol{M}$ lies along the [111] direction parallel to the O–A bond [Fig. 6(1)] and three more for (2) muon sites where $\boldsymbol{S}$ lies along the other three [111] directions [Fig. 6(2)]. Hence, the latter are three times as frequent and for the total field intensity B_μ, we obtain two triplets of distinct values, with expected amplitudes in the ratio of 1:3.

At high temperature, $\boldsymbol{B}_\mu=\boldsymbol{B}_L+\boldsymbol{B}_{hf}=\boldsymbol{B}_{hL}$ lies along one of the four {111} directions, with equal components $B_{hL}/\sqrt{(3)}$ in

the three Cartesian {100} directions. In order to justify a single experimental value B_μ of the total field intensity, one must seek for a single simultaneous solution B_{hL} of six second degree equations,

$$\frac{B_{hL}^2}{3} + \frac{2}{\sqrt{3}} B_{hL} \sum_{i=x,y,z} B_{di}^{\alpha j} + (B_d^{\alpha j})^2 - B_\mu^2 = 0, \qquad (3)$$

for $\alpha = a, b, c$ and $j = 1, 2$. Since the values of $B_d^{\alpha j}$ are all above 1 T and $\boldsymbol{B}_d^{\alpha j}$ have very different orientations, there is no such common solution (some of the equations do not even allow for a real solution), i.e., the single experimental value observed for $T > T_{II}$ cannot be justified by a localized muon picture.

Muons must therefore undergo fast diffusion above T_{II} and precess around the much smaller time-averaged field. The average over all the eight distinct 1 and 2 sites vanishes altogether because of the cubic symmetry and the single experimental field corresponds therefore simply to $\boldsymbol{B}_\mu = \boldsymbol{B}_L + \boldsymbol{B}_{hf} = \boldsymbol{B}_{hL}$ for all muons, whence we obtain $B_{hf} \approx 0.21$ T.

Electrostatic calculations support the possibility of a fast muon motion among equivalent sites which would produce this average: a, b, and c sites correspond to shallow minima, connected by a potential valley, visible in Fig. 6(3). This justifies tunneling among the minima, as well as higher temperature hopping to a nearby oxygen. Unconstrained fast hopping above 250 K takes place also in other transition metal oxides, such as orthoferrites,[25] cuprates,[26] and manganites.[22]

The same value of B_{hf} agrees with the experiment also for $T_I < T < T_{II}$, if one assumes that now muon diffusion is restricted to fast tunneling among local a, b, and c minima. This assumption, quite natural in view of the shallow barriers of Fig. 6(3), yields two average fields $\boldsymbol{B}_{\mu j} = \Sigma_{\alpha=a,b,c} \boldsymbol{B}_{\mu \alpha j}$, $j = 1, 2$, with moduli $B_{\mu 1} = 0.36$ T and $B_{\mu 2} = 0.43$ T and fractions in the ratio $f_2/f_1 = 3$, as it is indeed observed in Fig. 5 (squares and triangles).

The merging of $B_{\mu 1}$ and $B_{\mu 2}$ into $B'_{\mu 1}$ below T_R, where spin reorient, is also justified by the same assumptions, since for $\boldsymbol{S} \| [100]$ $(T < T_R)$, all oxygen ions in the magnetic cell become equivalent, yielding the same dipolar field values in the three minima a, b, and c, with vanishing local average by cubic symmetry. Hence, local tunneling predicts the average field $B'_{\mu 1} = B_{hL}$ for all muons, in agreement with observation (squares in Fig. 5).

Precisely, this field value, $B'_{\mu 1} = B_{hL}$, is detected also below T_V, down to $T = 0$. The same quantity may also be computed from $(3B_{\mu 2} + B_{\mu 1})/4$ for $T_R < T < T_{II}$ and directly from B_μ for $T > T_{II}$. We plot B_{hL} versus temperature in Fig. 7, together with a fit to the power law $B(T) = B_0(1 - T/T_N)^\beta$. By imposing[27] $T_N = 858$ K, we obtain $B_0 = 0.447$ T and $\beta = 0.22$ (the last parameter may be inaccurate, since T/T_N is limited to 0.34). The overall agreement firmly establishes our site assignment and dipolar calculations, validating the simple electrostatic criterion and the two-stage muon diffusion.

Finally, let us go back to the spin reorientation at T_R, around which a third field, $B_{\mu 3}$, is observed, with a strong temperature dependence. Its smooth decrease toward 0.2 T for $T \to T_V$ must arise from *fast* fluctuations among two distinct local field configurations, with temperature dependent relative probabilities. We tentatively identify the two configurations as due to different local spin orientations. Indeed for a muon inside a [001] domain bubble, the dipolar field vanishes. A static bubble within a larger [111] domain would also determine a cancellation of the Lorentz field, since a roughly equal but opposite term is provided by the boundaries of the bubble itself. Hence, the local field predicted by Eq. (2) would be $B_{\mu 3} = B_{hf} \approx 0.21$ T. If the [001] bubble is fast fluctuating in a [111] background, the muons may experience a temperature dependent average between the two static values: 0.21 T and $B_{\mu 1}$ (or $B_{\mu 2}$).

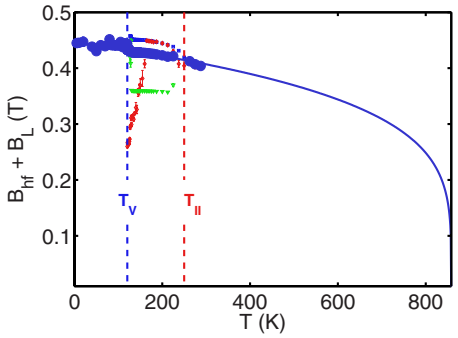

FIG. 7. (Color online) The sum $B_{hL} = B_L + B_{hf}$ (solid circles) with best fit to a power law (see text).

This simple model, therefore, brings forward the following picture: below $T_{II} = 150$ K, tiny bubbles of [001] spin orientation diffuse on a time scale $\Gamma^{-1} \ll 20$ ns, much shorter that the muon precession period. They are also characterized by a short coherence length ξ (the bubble radius). If Γ^{-1} increases as T_V is approached, it shifts the weight in the muon average field $B_{\mu 3}$ toward B_{hf}. This situation may well survive also below T_R, where a similar picture applies with exchanged roles: small bubbles of [111] inside a [001] domain also provide the cancellation of $\boldsymbol{B}_L$.

B. Below T_V

Let us consider now the range $T < T_V$, where the minima of the electrostatic potential $\phi_e(r)$ may become nonequivalent, depending on the local charge configuration (LCC) of the nearest B_{pcu} (Fig. 1). Therefore, in agreement with higher temperature findings, we assume that muons either tunnel among equivalent minima or reside at nonequivalent one.

We map the electrostatic potential $\phi_e(\boldsymbol{r})$ on $\mathcal{S}(r_\mu)$ for two different models: that originally due to Verwey, respecting Anderson condition, with localized Fe^{3+} and Fe^{2+} and that suggested by Wright *et al.*,[2] with localized charges $Fe^{+2.4}$ and $Fe^{+2.6}$, violating Anderson condition. The potential is evaluated on the small cluster of Fig. 1, which allows a finer scan in each LCC for both models. Note that, in view of the inherent approximations of a point-charge model, we are not trying to get a perfect correspondence between our calculations and the experimental data, and any attempt to determine fine details, such as the precise charge unbalance on each ion, would be beyond our scope. However, the approximate local field values and their muon fractions are already

TABLE II. Total field intensity, in T, at $T=0$ K for Verwey and Wright models (see text) for each LCC on B sites, labeled by three nn. Fe valences (in bold). Overline indicates average among three sites and asterisk between two sites only.

Model	Local charge configurations			
Verwey	**223**		**232 322**	
Fields (T)	1.14	0.70*	1.85	0.98*
Wright	**2.4 2.4 2.6**		**2.4 2.4 2.4**	
Fields (T)	1.11	0.71*	$\overline{0.45}$	
Expt. Fields (T)	1.09(3)	0.80(1)	0.447(5)	

sufficiently stringent constraints on our sums to validate classes of charge models.

Table II summarizes our findings for the two models, labeling each field value by the LCC of the B sites, nearest neighbor to the muon. If we disregard the finer details, due to slightly different muon site locations and different magnetic moments (Table I) in the two models, we recognize that the static values of $B_{\mu\alpha j}$ group around two values, $B_2=1.80(5)$ T and $B_3=1.10(5)$ T, where the quoted deviation accounts for the difference between models. The latter value agrees with $B'_{\mu 3}$, but the former (twice as frequent in the Verwey model) is never observed.

The condition for local muon tunneling is the presence of degenerate electrostatic potential minima. Figure 8 shows that in the Verwey model, the a,b muon minima are always degenerate (they are closest to a Fe^{2+} and a Fe^{3+} ions), whereas the absolute minimum is for the muon closest to two Fe^{2+} ions. Since there is no correlation between the direction of $\boldsymbol{M}\|[001]$ (it may be along $\hat{x}$, $\hat{y}$, or $\hat{z}$) and the vector joining the muon to the Fe^{3+} ion, the values listed in Table II are obtained by all permutations of a pairwise average, and by the residual static value, which, in turn, is equal either to B_2 or to B_3.

In the Wright model, muons must stop in the charge troughs of the charge density wave, i.e., around O_1 or O_2 in the basal plane of the cube shown in Fig. 1 (right). The former yields three equivalent muon minima, since its three nearest neighbor (nn) B ions are all $Fe^{2.4}$, hence locally tunneling muons. The latter yields an absolute minimum, with local field B_3, and a double-well tunneling muon where the average of the two differently oriented B_2 fields yields 0.71 T (Table II). The essential feature of a CDW along the c axis is the perfect correlation that it provides between the direction of the $O-Fe^{2.6}$ bond seen by the muon and that of the magnetic moments: they are all parallel to (001). This correlation grants the agreement with muon experiments and it is totally lost in the Verwey model.

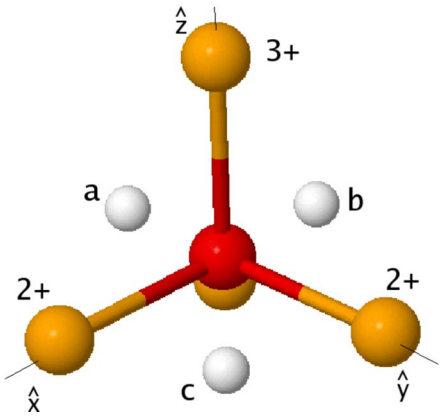

FIG. 8. (Color online) Muon sites (white) and Fe_B ions in the Verwey model below T_V; the spin, along [001], may lie nearly parallel to $\hat{x}$, $\hat{y}$, or $\hat{z}$.

V. CONCLUSIONS

In conclusion, we determine the muon location in Fe_3O_4 and we detect a muon motion partially correlated with charge localization. Our data show that there is a one-third fraction of muons still performing local tunneling around a fixed oxygen below T_V. Although this evidence does not provide full details about the local charge configurations, it implies that the charge of the second nearest neighbor ions to muon must be equal to nearly one-third of the muon sites. This statement is a direct violation of the Anderson condition. We also show that our findings are naturally reconciled with the structural model of Wright *et al.*[2] Since the two evidences are quite independent, one from k-space data and the other from r-space data, we provide strong support for the existence of a CDW below T_V. We further confirm a spin reorientation transition below 126 K, from $\boldsymbol{S}\|[111]$ to $\boldsymbol{S}\|[111]$, precursor to the Verwey transition, and around it, we deduce an inhomogeneous, dynamic phase separation in fractions of the sample.

ACKNOWLEDGMENTS

We thank G. Guidi and M. Riccò for discussions. We acknowledge the use of the GPS spectrometer, the help of the SμS, and of the accelerator staff of the Paul Scherrer Institut. Research funded under STREP OFSPIN, Nanofaber Laboratory, and NMI3 Access Program.

[1] A. Daoud-Aladine, J. Rodriguez-Carvajal, L. Pinsard-Gaudart, M. T. Fernandez-Diaz, and A. Revcolevschi, Phys. Rev. Lett. **89**, 097205 (2002).

[2] J. P. Wright, J. P. Attfield, and P. G. Radaelli, Phys. Rev. Lett. **87**, 266401 (2001).

[3] J. García, G. Subías, M. G. Proietti, H. Renevier, Y. Joly, J. L. Hodeau, J. Blasco, M. C. Sánchez, and J. F. Bérar, Phys. Rev. Lett. **85**, 578 (2000).

[4] J. García and G. Subías, J. Phys.: Condens. Matter **16**, R145 (2004).

[5] J. Coey and C. Chien, MRS Bull. **28**, 720 (2003).
[6] Z. Daihua, L. Zuqin, H. Song, L. Chao, L. Bo, M. Stewart, J. Tour, and Chongwu Zhou, Nano Lett. **4**, 2151 (2004).
[7] Y. Lu, J. Claydon, E. Ahmad, Y. Xu, M. Ali, B. Hickey, S. Thompson, J. Matthew, and K. Wilson, J. Appl. Phys. **97**, 10C313 (2005).
[8] P. Jin, B. Sung, W. Young, H. Jong, S. K. W. Ki, O. Chae, H. Chang, and H. Myoung, Appl. Phys. Lett. **83**, 1590 (2003).
[9] I. Leonov, A. N. Yaresko, V. N. Antonov, and V. I. Anisimov, Phys. Rev. B **74**, 165117 (2006).
[10] E. J. Verwey and P. W. Haayman, Physica (Utrecht) **8**, 979 (1941).
[11] G. Shirane, S. Chikazumi, J. Akimitsu, K. Chiba, M. Matsui, and Y. Fujii, J. Phys. Soc. Jpn. **39**, 949 (1975).
[12] F. Walz, J. Phys.: Condens. Matter **14**, R285 (2002).
[13] P. Anderson, Phys. Rev. **102**, 1008 (1956).
[14] J. P. Wright, J. P. Attfield, and P. G. Radaelli, Phys. Rev. B **66**, 214422 (2002).
[15] G. Subías, J. García, J. Blasco, M. Grazia Proietti, H. Renevier, and M. Concepcion Sánchez, Phys. Rev. Lett. **93**, 156408 (2004).
[16] P. Novak, H. Stepankova, J. Englich, J. Kohout, and V. A. M. Brabers, Phys. Rev. B **61**, 1256 (2000).
[17] M. Mizoguchi, J. Phys. Soc. Jpn. **70**, 2333 (2001).
[18] M. Bimbi, G. Allodi, R. D. Renzi, G. Mazzoli, H. Berger, and A. Amato, Physica B **374-375**, 51 (2006).
[19] C. Boekema, R. L. Lichti, V. A. M. Brabers, A. B. Denison, D. W. Cooke, R. H. Heffner, R. L. Hutson, M. Leon, and M. E. Schillaci, Phys. Rev. B **31**, 1233 (1985).
[20] C. Boekema, R. L. Lichti, K. C. B. Chan, V. A. M. Brabers, A. B. Denison, D. W. Cooke, R. H. Heffner, R. L. Hutson, and M. E. Schillaci, Phys. Rev. B **33**, 210 (1986).
[21] M. Bimbi, G. Allodi, R. D. Renzi, C. Mazzoli, and H. Berger (unpublished).
[22] M. C. Guidi, G. Allodi, R. De Renzi, G. Guidi, M. Hennion, L. Pinsard, and A. Amato, Phys. Rev. B **64**, 064414 (2001).
[23] D. Owoc, J. Przewoznik, A. Kozlowski, Z. Kakol, A. Wiechec, and J. Honig, Physica B **359-361**, 1339 (2005).
[24] A. Schenck, *Muon Spin Rotation: Principles and Applications in Solid State Physics* (Adam Hilger, Bristol, 1985).
[25] E. Holzschuh, A. B. Denison, W. Kundig, P. F. Meier, and B. D. Patterson, Phys. Rev. B **27**, 5294 (1983).
[26] A. Keren, L. P. Le, G. M. Luke, B. J. Sternlieb, W. D. Wu, Y. J. Uemura, S. Tajima, and S. Uchida, Phys. Rev. B **48**, 12926 (1993).
[27] C. Boekema, Hyperfine Interact. **17-19**, 305 (1984).